Published in "Physical Review E 88(4): 042303, 2013"
which should be cited to refer to this work.

Normal-stress coefficients and rod climbing in colloidal dispersions

T. F. F. Farage, J. Reinhardt, and J. M. Brader*
Department of Physics, University of Fribourg, CH-1700 Fribourg, Switzerland
(Received 12 July 2013; revised manuscript received 11 September 2013; published 7 October 2013)

We calculate tractable microscopic expressions for the low-shear normal-stress coefficients of colloidal dispersions. Although restricted to the low rate regime, the presented formulas are valid for all volume fractions below the glass transition and for any interaction potential. Numerical results are presented for a system of colloids interacting via a hard-core attractive Yukawa potential, for which we explore the interplay between attraction strength and volume fraction. We show that the normal-stress coefficients exhibit nontrivial features close to the critical point and at high volume fractions in the vicinity of the reentrant glass transition. Finally, we exploit our formulas to make predictions about rod-climbing effects in attractive colloidal dispersions.

I. INTRODUCTION

Complex fluids, such as colloidal dispersions, exhibit a nontrivial response when submitted to an externally applied flow. Depending on the thermodynamic state point, the strain, and the strain rate, nonlinear changes in macroscopic quantities may be observed (e.g., thinning or thickening of the shear viscosity [1,2]). In contrast to Newtonian fluids, complex fluids typically exhibit nonzero values of the first and second normal-stress differences. These rheological functions are of a higher order than the familiar shear viscosity, in the sense that their lowest-order contribution to the flow response is quadratic in the shear rate [3], and are responsible for many physical phenomena, such as the Weissenberg ("rod-climbing") effect in Couette rheometry [4–8] or the extrudate swell of fluids emerging from a tube [9].

The first normal-stress difference N_1 is defined for shear flow as the difference between normal stresses in the flow and gradient direction, respectively, whereas the second normal-stress difference N_2 is given by the difference between normal stresses in the gradient and vorticity (neutral) direction. In Cartesian coordinates with flow in the x direction and shear gradient in the y direction, this yields $N_1 \equiv \sigma_{xx} - \sigma_{yy}$ and $N_2 \equiv \sigma_{yy} - \sigma_{zz}$, where the σ_{ij} are stress tensor elements.[1] In experiment, the magnitudes of N_1 and N_2 determine the normal force acting on the plates of a rheometer, although the details of this relationship will depend on the geometry of the applied flow (e.g., cone-plate, plate-plate) and on boundary conditions [5]. For example, in a cone-plate rheometer, N_1 is directly proportional to the force per unit area acting on the plate, which tends to push the plates apart if $N_1 > 0$, but tends to pull them together if $N_1 < 0$ [1]. The existence of normal stresses can be viewed as a consequence of distortion of the pair correlations away from their equilibrium forms.

The importance of normal stresses for the flow of non-Newtonian fluids is most clearly demonstrated by the phenomenon of rod climbing [4], whereby the fluid climbs up a rotating shaft, leading to a dramatic distortion of the meniscus profile relative to its quiescent form. For polymeric systems, this effect is attributed to the existence of a tension along the (circular) lines of flow, which pulls the liquid radially inwards and, consequently, as a result of molecular crowding in the vicinity of the rod surface, upwards against gravity. The magnitude of the normal stresses characterizing flow-line tension in polymeric liquids (sometimes referred to as "hoop stresses") is often of comparable magnitude to the shear stresses acting in the system. Experimentally, the rod climbing exhibited by non-Newtonian fluids can be exploited to characterize nonlinear material properties. In particular, the low-shear-rate limiting values of the first and second normal-stress coefficients (respectively, $\Psi_1 \equiv N_1/\dot{\gamma}^2$ and $\Psi_2 \equiv N_2/\dot{\gamma}^2$, where $\dot{\gamma}$ is the shear rate) can be obtained from observing the shape of the meniscus at the rod surface [5,10]. This method avoids the experimental difficulties associated with measuring small stress values directly. Recently, a promising alternative technique based on active microrheology has been proposed to simultaneously measure the first and second normal-stress coefficients of a complex fluid [11].

On the basis of existing rheological data for suspensions of repulsive spherical particles, it appears that these systems usually exhibit a value of N_1 which is positive and at least a factor of three larger than that of N_2, with the latter quantity being negative [1]. An exception to this rule is found at high-shear rates, where theory [12], Stokesian dynamics simulations [13], and experiments [14] have all demonstrated that a change of sign of N_1 from a positive to a negative value can arise when the system enters the shear-thickening regime. Although consensus has yet to be reached, it seems likely that this behavior is connected to the formation of lubrication-aggregated colloidal "hydroclusters" [15,16]. A sign change in N_1 as a function of rate can also be found in more complex systems, such as polymeric liquid crystals [1], or in attractive emulsions near the glass transition under shear flow [17]. In the latter case, the onset of negative N_1

*joseph.brader@unifr.ch

[1]The sign convention for both the hydrostatic pressure and the components of the deviatoric stress tensor is often a source of confusion. In the present work, we follow Refs. [1,2,5], for which the hydrostatic pressure exerted on a fluid element by its surrounding is negative (compression) and tensile stress is positive. Some authors prefer to keep both the hydrostatic pressure and the deviatoric stress components positive in compression (see p. *vii* of the preface in [6]).

coincides with the formation of rolling cylindrical flocs along the vorticity direction. In complete contrast to the above, a purely negative N_1 is observed in extended, space-spanning networks, such as semiflexible biopolymer gels, regardless of the deformation rate [18].

Understanding the whole rheology of colloidal dispersions from the underlying microscopic mechanisms within a unique theoretical framework is a formidable task in nonequilibrium statistical mechanics [19], even for the simplest case of monodisperse spherical particles. Indeed, a full description of the many-body dynamics of colloidal particles in a dispersion under flow should incorporate the complex interplay between Brownian motion, potential interactions, solvent-mediated hydrodynamic interactions, and the geometry of the imposed (time-dependent) flow [20]. Although an all-encompassing constitutive theory is still lacking, significant progress has been made in recent decades. Early attempts employed a fluctuating diffusion equation to calculate the nonequilibrium static structure factor of dilute charged suspensions under shear, from which zero-shear limit expressions for the viscosity and the normal-stress differences were obtained [21,22]. An alternative approach, valid at low volume fraction, is to numerically solve the two-particle Smoluchowski equation for the distorted pair correlations, from which the stress tensor components can be calculated [3,12].

More recently, the *integration through transients* (ITT) approach has been developed which enables the derivation of exact generalized Green-Kubo formulas, namely, expressions relating average quantities to time integrals over microscopic correlation functions [23]. Mode-coupling-type approximations to these exact results (ITT-MCT) then lead to closed expressions for the macroscopic stress tensor and microscopic time-correlation functions [23–25]. The only required input to the ITT-MCT expressions are the volume fraction and static structure factor, which serves as proxy for the bare colloidal interaction potential.

A central feature of this approach is that it captures the nonequilibrium transition between a fluid and an amorphous solid.[2] When applied to calculate the stress tensor, this theory provides a fully tensorial constitutive equation [26]. In principle, this makes possible the calculation of the main rheological functions of a colloidal dispersion under arbitrary time-dependent flow, for any imposed interaction potential and volume fraction, either above or below the glass transition. In practice, the simultaneous presence of spatial anisotropy and logarithmic time scales hinders numerical implementation: full solutions in three spatial dimensions have not yet been achieved. Progress has been made in solving the theory for two-dimensional model fluids [27,28] and the available numerical results show that the ITT-MCT approach makes sensible predictions, in qualitative agreement with Brownian dynamics simulation data.

In order to both facilitate a numerical solution and expose the essential physics of the microscopic theory, simplified schematic models have been proposed [29,30], which aim to provide a simpler set of equations with the essential mathematical structure of the microscopic theory. Recent applications of this simplified theory have shown that it provides a consistent and physically robust approach to the phenomenology of glassy rheology [31–34]. However, in resorting to a schematic description of the full theory [25], one loses all microscopic spatial information.

In this paper, we start from the fully microscopic, three-dimensional ITT-MCT constitutive equation [25] and analyze the normal-stress coefficients, Ψ_1 and Ψ_2, which emerge in the low-shear-rate limit. As these coefficients are independent of the shear rate, they represent genuine material functions, with a status similar to the familiar zero-shear viscosity. By limiting our investigations to the low rate regime, we can extract from the full constitutive model [25] explicit and tractable mode-coupling formulas for the normal-stress coefficients, which retain wave-vector dependence and require only the volume fraction and static structure factor as input. This enables us to investigate the dependence of both Ψ_1 and Ψ_2 on the details of the interparticle interaction. As an illustrative example, we focus on a system of colloidal particles interacting via a hard-core attractive Yukawa (HCAY) potential, which is known to exhibit a reentrant glass transition at high volume fractions as a function of the attraction strength [35]. The calculated normal-stress coefficients then allow us to make predictions regarding the rod-climbing effect in this model system, namely, the dependence of the surface profile on both the volume fraction and the strength of the interparticle attraction.

The paper is organized as follows: In Sec. II A, we outline the formal integration through transients approach, which leads to an exact generalized Green-Kubo relation for the stress tensor. In Sec. II B, the normal-stress coefficients are discussed in the context of the Green-Kubo formalism. In Sec. II C, we summarize the mode-coupling constitutive equation of [25] which approximates the previously developed exact generalized Green-Kubo expressions. In Sec. II D, we exploit the constitutive equation to derive formulas for the low-shear-rate limit of the three main rheological functions (i.e., the viscosity and the first and second normal-stress coefficients). In Sec. III, we apply our theory to investigate the dependence of the normal-stress coefficients on volume fraction and attraction strength for the HCAY system. In Sec. III C, we use the calculated Ψ_1 and Ψ_2 to predict the surface profiles which would be obtained in a rod-climbing experiment. Finally, in Sec. IV, we summarize our results and provide an outlook for future work.

II. THEORY

A. Integration through transients

We consider a system of spherical colloidal particles, driven into a steady nonequilibrium state by an imposed velocity gradient matrix $\boldsymbol{\kappa}$, whose form we initially do not specify. For a system of N Brownian particles dispersed in a solvent, interacting through a potential $U_N(\{\mathbf{r}_i\})$ (where $\{\mathbf{r}_i\} \equiv \{\mathbf{r}_1, \mathbf{r}_2, \ldots, \mathbf{r}_N\}$, with $\mathbf{r}_i$ indicating the position of the ith particle), the equation of motion for the probability distribution $\Psi(\{\mathbf{r}_i\},t)$ is given by

$$\frac{\partial \Psi(\{\mathbf{r}_i\},t)}{\partial t} = \hat{\Omega}\, \Psi(\{\mathbf{r}_i\},t), \tag{1}$$

[2] Shear thickening is not captured by the theory since hydrodynamic interactions are neglected.

where $\hat{\Omega}$ is the Smoluchowski operator,

$$\hat{\Omega} = \sum_{i=1}^{N} \nabla_i \cdot [D_0(\nabla_i - \beta \mathbf{F}_i) - \boldsymbol{\kappa} \cdot \mathbf{r}_i], \tag{2}$$

with $\beta = (k_B T)^{-1}$, bare diffusion coefficient D_0, and the direct force $\mathbf{F}_i = -\nabla_i U_N$ acting on particle i. Many-body hydrodynamic interactions have not been taken into account. A formal solution of (1) is given by

$$\Psi(\{\mathbf{r}_i\}, t \to \infty) = \Psi_{\rm eq}(\{\mathbf{r}_i\}) + \beta V \int_0^\infty ds\, \Psi_{\rm eq}(\{\mathbf{r}_i\}) \boldsymbol{\kappa} : \hat{\boldsymbol{\sigma}}\, e^{s\hat{\Omega}^\dagger}, \tag{3}$$

where $\Psi_{\rm eq}(\{\mathbf{r}_i\})$ is the equilibrium Boltzmann distribution function, $\hat{\sigma}_{\alpha\beta} = -(1/V)\sum_{i=1}^{N} F_\alpha^i r_\beta^i$, with $\alpha, \beta = \{x, y, z\}$, are the components of the potential part of the stress tensor $\hat{\boldsymbol{\sigma}}$,[3] and V is the volume of the system. The full contraction is defined as $\mathbf{A} : \mathbf{B} \equiv \sum_{\alpha,\beta} A_{\alpha\beta} B_{\beta\alpha}$ and the adjoint Smoluchowski operator is given by

$$\hat{\Omega}^\dagger = \sum_{i=1}^{N} [D_0(\nabla_i + \beta \mathbf{F}_i) + \mathbf{r}_i \cdot \boldsymbol{\kappa}^T] \cdot \nabla_i. \tag{4}$$

The solution (3) is the fundamental result of the ITT approach and expresses the nonequilibrium probability distribution function as an integral over the entire transient flow history.

Nonequilibrium averages of any phase-space quantity $f(\{\mathbf{r}_i\})$ can thus be expressed as

$$\langle f \rangle_{\rm neq} = \langle f \rangle + \beta V \int_0^\infty ds \left\langle \boldsymbol{\kappa} : \hat{\boldsymbol{\sigma}}\; e^{s\hat{\Omega}^\dagger} f \right\rangle, \tag{5}$$

where $\langle \cdot \rangle_{\rm neq}$ denotes an average over the nonequilibrium probability distribution function (3) and $\langle \cdot \rangle$ is a standard equilibrium average. If we take $f = \hat{\boldsymbol{\sigma}}$, then (5) reads

$$\boldsymbol{\sigma} \equiv \langle \boldsymbol{\sigma} \rangle_{\rm neq} = \langle \hat{\boldsymbol{\sigma}} \rangle + \beta V \int_0^\infty ds \left\langle \boldsymbol{\kappa} : \hat{\boldsymbol{\sigma}}\; e^{s\hat{\Omega}^\dagger} \hat{\boldsymbol{\sigma}} \right\rangle, \tag{6}$$

which is an exact Green-Kubo-type relation for the stress tensor, expressed as a time integral over the flow history of the microscopic stress autocorrelation function. The term $\langle \hat{\boldsymbol{\sigma}} \rangle$ yields an isotropic contribution, namely, the interaction-induced excess (over ideal) contribution to the equilibrium pressure, which contributes to neither the viscosity nor the normal-stress coefficients under consideration here.

B. Normal-stress coefficients

For the special case of steady shear flow, (6) provides a formal result for the first normal-stress difference,

$$N_1 = \beta V \dot{\gamma} \int_0^\infty dt \left\langle \hat{\sigma}_{xy}\; e^{t\hat{\Omega}^\dagger} (\hat{\sigma}_{xx} - \hat{\sigma}_{yy}) \right\rangle, \tag{7}$$

where we have used the fact that $\langle \hat{\sigma}_{xx} - \hat{\sigma}_{yy} \rangle = 0$. Using the Taylor expansion

$$e^{\hat{x}+\alpha\hat{y}} = e^{\hat{x}} + \alpha \left[\frac{d}{d\alpha} e^{\hat{x}+\alpha\hat{y}} \right]_{\alpha=0} + \cdots, \tag{8}$$

which is valid for arbitrary operators $\hat{x}$ and $\hat{y}$, where α is a scalar parameter, we can expand the right-hand side of (7) to quadratic order in $\dot{\gamma}$, yielding

$$N_1 = \beta V \dot{\gamma} \int_0^\infty dt \left\langle \hat{\sigma}_{xy} e^{t\hat{\Omega}_{\rm eq}^\dagger} (\hat{\sigma}_{xx} - \hat{\sigma}_{yy}) \right\rangle + \beta V \dot{\gamma}^2 \int_0^\infty dt \left\langle \hat{\sigma}_{xy} \left[\frac{d}{d\dot{\gamma}}\; e^{t\hat{\Omega}^\dagger} \right]_{\dot{\gamma}=0} (\hat{\sigma}_{xx} - \hat{\sigma}_{yy}) \right\rangle. \tag{9}$$

The first term of (9) vanishes identically, due to symmetry (N_1 is independent of the direction of the shear flow). Introducing the strain $\gamma = \dot{\gamma} t$, the nonvanishing second term in (9) can be rewritten as

$$N_1 = \beta V \dot{\gamma}^2 \int_0^\infty dt\, t \left\langle \hat{\sigma}_{xy}(0) \frac{d}{d\gamma} [\hat{\sigma}_{xx}(t) - \hat{\sigma}_{yy}(t)]_{\gamma=0} \right\rangle. \tag{10}$$

The infinitesimal strain tensor, $\boldsymbol{\varepsilon} = (\boldsymbol{\kappa} + \boldsymbol{\kappa}^T) t/2$, is a standard deformation measure from elasticity theory. In the present case of simple shear, the flow-gradient elements of this tensor are given by $\varepsilon_{xy} = \varepsilon_{yx} = \gamma/2$, such that (10) can be expressed in the alternative form

$$N_1 = \frac{\beta V \dot{\gamma}^2}{2} \int_0^\infty dt\, t \left\langle \hat{\sigma}_{xy}(0) \frac{d}{d\varepsilon_{xy}} [\hat{\sigma}_{xx}(t) - \hat{\sigma}_{yy}(t)]_{\varepsilon_{xy}=0} \right\rangle. \tag{11}$$

For a general anisotropic material, Hooke's law can be written as $\sigma_{ij} = \sum_{k,l} C_{ijkl}\, \varepsilon_{lk}$, where the C_{ijkl} are the components of a fourth-order tensor, $\boldsymbol{C}$, called the stiffness or elasticity tensor, with $i, j, k, l = \{x, y, z\}$. These components are the elastic constants of the material. By analogy with these continuum definitions, we propose to define *fluctuating elastic constants*

$$\hat{C}_{ijkl}(t) \equiv \left(\frac{d\hat{\sigma}_{ij}(t)}{d\varepsilon_{lk}} \right)_{\varepsilon_{lk}=0}. \tag{12}$$

Substitution of (12) into (11) and division of the resulting expression by $\dot{\gamma}^2$ leads to a compact result for the first normal-stress coefficient,

$$\Psi_1 = \frac{\beta V}{2} \int_0^\infty dt\, t \langle \hat{\sigma}_{xy}(0) [\hat{C}_{xxxy}(t) - \hat{C}_{yyxy}(t)] \rangle. \tag{13}$$

Entirely analogous reasoning leads also to an expression for the second normal-stress coefficient

$$\Psi_2 = \frac{\beta V}{2} \int_0^\infty dt\, t \langle \hat{\sigma}_{xy}(0) [\hat{C}_{yyxy}(t) - \hat{C}_{zzxy}(t)] \rangle. \tag{14}$$

Equations (13) and (14) provide a microscopic interpretation of the macroscopic normal-stress coefficients as time integrals over equilibrium correlations between a shear stress fluctuation $\hat{\sigma}_{xy}$ and the fluctuating elastic constants.

The formal expressions (13) and (14) for the material functions Ψ_1 and Ψ_2 can be compared and contrasted with

[3] In a liquid, it is the potential part of the stress tensor which dominates, whereas in gaseous systems, the kinetic part is the main contribution to the stress.

the standard result for the zero-shear viscosity [36],

$$\eta_0 = \beta V \int_0^\infty dt \langle \hat{\sigma}_{xy}(0)\hat{\sigma}_{xy}(t)\rangle. \tag{15}$$

Equations (13)–(15) have in common that the correlation function to be integrated involves the fluctuating shear stress element $\hat{\sigma}_{xy}(0)$, which recognizes that the applied flow is a shearing motion in the x-y plane. The appearance of the fluctuating elastic constants in the correlation functions required for (13) and (14), as opposed to the simple stress element $\hat{\sigma}_{xy}(t)$ as in (15), expresses the fact that interparticle interactions are responsible for converting shearing motion of the fluid into normal stresses.

For compressible isotropic media, the elastic constants C_{ijkl} are given by $C_{ijkl} = \lambda\delta_{ij}\delta_{kl} + \mu(\delta_{ik}\delta_{jl} + \delta_{il}\delta_{jk})$ (see Ref. [37]), which implies that

$$\langle \hat{C}_{xxxy}\rangle = 0, \quad \langle \hat{C}_{yyxy}\rangle = 0, \quad \langle \hat{C}_{zzxy}\rangle = 0, \tag{16}$$

are satisfied by the fluctuating elastic constants in equilibrium.

C. The MCT constitutive equation

The application of MCT-type projection operator methods to approximate the stress autocorrelation function in (6) leads to a closed microscopic constitutive equation for arbitrary steady flow [26],

$$\boldsymbol{\sigma} = \frac{1}{\beta 32\pi^3}\int_0^\infty dt \int d\mathbf{k}\left\{\frac{\partial}{\partial t}[\mathbf{k}\cdot\mathbf{B}(t)\cdot\mathbf{k}]\mathbf{kk}\right\} \times \left\{\left[\frac{S_k' S_{k(t)}'}{kk(t)S_k^2}\right]\Phi^2_{\mathbf{k}(t)}(t)\right\}, \tag{17}$$

where $\mathbf{kk}$ is a dyadic product with components $(\mathbf{kk})_{\alpha\beta} = k_\alpha k_\beta$, and S_k and S_k' are the *equilibrium* static structure factor and its derivative, respectively.

The Finger tensor $\mathbf{B}(t)$ is a standard nonlinear deformation measure [38], which is defined via the deformation tensor $\mathbf{E}(t)$ according to

$$\mathbf{B}(t) \equiv \mathbf{E}(t)\cdot\mathbf{E}^T(t) = e^{t\boldsymbol{\kappa}}\cdot e^{t\boldsymbol{\kappa}^T}. \tag{18}$$

The time-dependent wave vectors in (17) are the reverse-advected wave vectors, $\mathbf{k}(t) \equiv \mathbf{k}\cdot\mathbf{E}(t) = \mathbf{k}\cdot e^{t\boldsymbol{\kappa}}$, and their presence in the microscopic constitutive equation (17) is a consequence of translational invariance for spatially homogeneous flows. External flow thus enters (17) via the Finger tensor as well as the (magnitude of the) reverse-advected wave vectors, in a nontrivial way. Finally, the function $\Phi_{\mathbf{k}(t)}(t)$ is the normalized transient density correlator, defined as the equilibrium average

$$\Phi_{\mathbf{k}(t)}(t) \equiv \frac{\langle \rho^*_{\mathbf{k}(t)} e^{t\cdot\hat{\Omega}^\dagger}\rho_{\mathbf{k}}\rangle}{NS(k)}. \tag{19}$$

Mode-coupling-type approximations to this quantity yield a closed equation of motion for the density correlator,

$$\dot{\Phi}_{\mathbf{q}}(t) + \Gamma_{\mathbf{q}}(t)\left[\Phi_{\mathbf{q}}(t) + \int_0^t dt' m_{\mathbf{q}}(t,t')\dot{\Phi}_{\mathbf{q}}(t')\right] = 0, \tag{20}$$

where $\Gamma_{\mathbf{q}}(t) \equiv D_0\,\bar{q}^2(t)/S_{\bar{q}(t)}$ is the initial decay rate, with $\bar{q}$ being the magnitude of the advected wave vector $\bar{\mathbf{q}}(t) \equiv \mathbf{q}\cdot e^{-t\boldsymbol{\kappa}}$. The memory kernel $m_{\mathbf{q}}(t,t')$ entering in the equation of motion (20) is given by

$$m_{\mathbf{q}}(t,t') = \frac{\rho}{16\pi^3}\int d\mathbf{k}\frac{S_{\bar{q}(t)}S_{\bar{k}(t')}S_{\bar{p}(t')}}{\bar{q}^2(t')\bar{q}^2(t)} \times V_{\mathbf{qkp}}(t')V_{\mathbf{qkp}}(t)\Phi_{\bar{\mathbf{k}}(t')}(t,t')\Phi_{\bar{\mathbf{p}}(t')}(t,t'), \tag{21}$$

where $\mathbf{p} = \mathbf{q} - \mathbf{k}$, and the vertex functions are given by

$$V_{\mathbf{qkp}}(t) = \bar{\mathbf{q}}(t)\cdot[\bar{\mathbf{k}}(t)c_{\bar{k}(t)} + \bar{\mathbf{p}}(t)c_{\bar{p}(t)}], \tag{22}$$

with the Ornstein-Zernike direct correlation function $\rho c_k = 1 - (1/S_k)$.

Equations (17)–(22) thus form a closed constitutive theory, where the only input quantities are the imposed flow $\boldsymbol{\kappa}$ and the static structure factor S_k. Calculation of the latter requires the interaction potential U_N and the volume fraction of the particles, $\varphi \equiv N(4/3)\pi R^3/V$, with R the radius of a particle. Although hydrodynamic interactions are absent in the above microscopic description, the constitutive equation (17) accounts for the competition between the slowing down of the structural relaxation with increasing volume fraction, which eventually leads to glassy arrest, and the shear-induced enhancement of relaxation.

D. Low-shear-rate expansion and formulas

The low-shear-rate limit of the stress tensor may be obtained by expanding the constitutive equation (17) as a power series in $\dot{\gamma}$. We henceforth restrict our considerations to a simple shear with flow in the x direction and gradient in the y direction, for which the velocity gradient tensor is given by

$$(\boldsymbol{\kappa})_{\alpha\beta} = \delta_{x\alpha}\delta_{y\beta}\dot{\gamma}. \tag{23}$$

Substitution of (23) into (18), and noting that $\boldsymbol{\kappa}^2 = \mathbf{0}$, yields the Finger tensor

$$\mathbf{B}(t) = \begin{pmatrix} 1+\dot{\gamma}^2t^2 & \dot{\gamma}t & 0 \\ \dot{\gamma}t & 1 & 0 \\ 0 & 0 & 1 \end{pmatrix}, \tag{24}$$

which allows us to directly calculate the time derivative in the first factor of the integrand in (17), namely,

$$\frac{\partial}{\partial t}[\mathbf{k}\cdot\mathbf{B}(t)\cdot\mathbf{k}] = 2\dot{\gamma}^2tk_x^2 + 2\dot{\gamma}k_xk_y. \tag{25}$$

A further source of shear-rate dependence in the integrand of (17) is the ratio $S_{k(t)}'/k(t)$. Expansion in $\dot{\gamma}$ yields

$$\frac{S_{k(t)}'}{k(t)} = \frac{S_k'}{k} + \dot{\gamma}\frac{d}{d\dot{\gamma}}\left[\frac{S_{k(t)}'}{k(t)}\right]\Bigg|_{\dot{\gamma}=0} + O(\dot{\gamma}^2), \tag{26}$$

with

$$\frac{d}{d\dot{\gamma}}\left[\frac{S_{k(t)}'}{k(t)}\right]\Bigg|_{\dot{\gamma}=0} = \frac{(kS_k'' - S_k')}{k^3}k_xk_yt, \tag{27}$$

where we have used the explicit form of the reverse-advected wave vector under shear, $\mathbf{k}(t) = \mathbf{k} + \dot{\gamma}tk_x$. Using Eqs. (25)–(27) in (17), and approximating the density correlator $\Phi_{\mathbf{k}(t)}(t)$ by its quiescent form $\Phi_k(t)$, yields to second order in the shear

rate the following expression for the ITT-MCT stress tensor:

$$\boldsymbol{\sigma} = \frac{1}{\beta 16\pi^3}\int_0^\infty dt \int d\mathbf{k}\,\mathbf{kk}\Big\{\dot\gamma k_x k_y\left(\frac{S_k'}{S_k}\right)^2\frac{1}{k^2}\Phi_k^2(t) + \dot\gamma^2 k_x^2\left(\frac{S_k'}{S_k}\right)^2\frac{1}{k^2}\Phi_k^2(t)t + \dot\gamma^2 k_x^2 k_y^2\left(\frac{S_k'}{S_k^2}\right)\frac{1}{k^4}(kS_k''-S_k')\Phi_k^2(t)\,t\Big\}. \tag{28}$$

Extracting from (28) the stress components of interest and integrating in $\mathbf{k}$ space, we obtain the main three viscometric functions in the low-shear-rate limit, namely, the viscosity,

$$\eta_0 \equiv \frac{\sigma_{xy}}{\dot\gamma} = \frac{1}{60\beta\pi^2}\int_0^\infty dt\int_0^\infty dk\; k^4\left(\frac{S_k'}{S_k}\right)^2\Phi_k^2(t), \tag{29}$$

the first normal-stress coefficient,

$$\Psi_1 \equiv \frac{N_1}{\dot\gamma^2} \equiv \frac{\sigma_{xx}-\sigma_{yy}}{\dot\gamma^2} = \frac{1}{30\beta\pi^2}\int_0^\infty dt\int_0^\infty dk\; k^4\left(\frac{S_k'}{S_k}\right)^2\Phi_k^2(t)t, \tag{30}$$

and the second normal-stress coefficient,

$$\Psi_2 \equiv \frac{N_2}{\dot\gamma^2} \equiv \frac{\sigma_{yy}-\sigma_{zz}}{\dot\gamma^2} = \frac{1}{210\beta\pi^2}\int_0^\infty dt\int_0^\infty dk\; k^4\left(\frac{S_k'}{S_k^2}\right)(kS_k''-S_k')\Phi_k^2(t)t. \tag{31}$$

Equation (29) is a well-known expression for the zero-shear-rate viscosity [36,39], whereas (30) and (31) are derived here. We note that the singular behavior of the flow distorted structure factor [40] does not play a role, except in the immediate vicinity of the critical point.

The key feature of the mode-coupling results (29)–(31) is that they enable parameter-free prediction of the most relevant rheological quantities for a colloidal system at any volume fraction (below the glass transition) and subject to an arbitrary interaction potential. The accuracy of the predictions will, of course, ultimately depend upon the reliability of the approximations employed. The quiescent density correlator required as input is isotropic and readily calculable using established numerical algorithms, thus avoiding the essential numerical difficulty which hinders solution of the full constitutive theory for three-dimensional systems. As we will demonstrate in Sec. III, the appropriate signs of the normal-stress coefficients naturally arise from (30) and (31), namely, $\Psi_1 > 0$ and $\Psi_2 < 0$, as well as their expected relative magnitude.

III. SHORT-RANGE ATTRACTIVE COLLOIDS

Adding an attractive component to the hard-sphere interaction potential supplements the well-known first-order crystallization transition by a colloidal liquid-gas transition, ending in a critical point. If the attraction is of sufficiently short range, then dynamic arrest to either an attractive glass or gel state may occur (see [41], and the references therein, for a review). Indeed, MCT predictions, later confirmed by simulations and experiments, revealed the existence of a reentrant glass transition as a function of attraction strength in dense suspensions [35].

The familiar *repulsive* glassy state is obtained by increasing the volume fraction of polydisperse hard-sphere particles beyond a critical volume fraction. This leads to an arrested state for which the motion of any particle on a distance greater than a few percent of its radius is hindered by the neighboring particles forming a cage around it. For systems with an additional short-range attraction, an attractive glass or gel state can be reached by reducing the temperature at intermediate ($\varphi > 40\%$) or low volume fraction, respectively.

In the remainder of this section, we study the low-shear-rate rheology of a system of colloidal particles interacting via a HCAY potential. In addition to providing a simple model for describing suspensions found in industrial [42] and biological processes [43], the fact that the phase diagram of the quiescent HCAY model presents both colloidal glass and gel transitions [44] makes this a system of fundamental interest.

A. Phase diagram

The HCAY interaction potential between two particles separated by a distance r is given by

$$\beta u(r) = \begin{cases} \infty, & 0 < r < \sigma \\ -\frac{K}{r/\sigma}e^{-b(r/\sigma-1)}, & \sigma < r, \end{cases}$$

where the dimensionless parameter K determines the depth of the attractive well, whereas the reduced screening parameter b sets the range of the attraction. The colloid diameter is denoted by σ. In the present work, we employ the value $b = 12$, as this choice generates a phase diagram exhibiting all the generic features of the model.

In Fig. 1, we show the equilibrium spinodal and nonequilibrium glass-gel transition lines. The static structure factor used to calculate the spinodal and as input to our mode-coupling approximations was calculated within the mean-spherical closure of the Ornstein-Zernike equation [45]. Despite the fact that we consider a monodisperse system, the physics of crystallization has no influence on the results to be presented in this work; neither the mean-spherical approximation nor the mode-coupling theory are capable of capturing the freezing transition. The nonequilibrium phase boundary was obtained using a bisection method, based on repeated numerical solution of (20)–(22) in the zero-shear-rate limit. To decide whether a state point is fluid or glassy, the long-time limits $\Phi_q(t\to\infty)$ of the transient density correlators were determined by solving the corresponding algebraic equation provided by MCT, and checked for nonzero values (see also the appendix in [44]). The time dependence of the transient density correlators was calculated using standard algorithms [46] on a wave-vector grid with 250 k values at a grid spacing of 0.3. Finite differences have been used to approximate the derivatives of the structure factor. The horizontal and vertical dotted lines in Fig. 1 indicate paths through the phase diagram along which we display results for the viscosity and normal-stress coefficients.

B. Rheological functions: Results

Figure 2 shows the volume fraction dependence of the zero-shear viscosity η_0 and the first and second normal-stress coefficients Ψ_1 and Ψ_2, at different potential depths K (as indicated

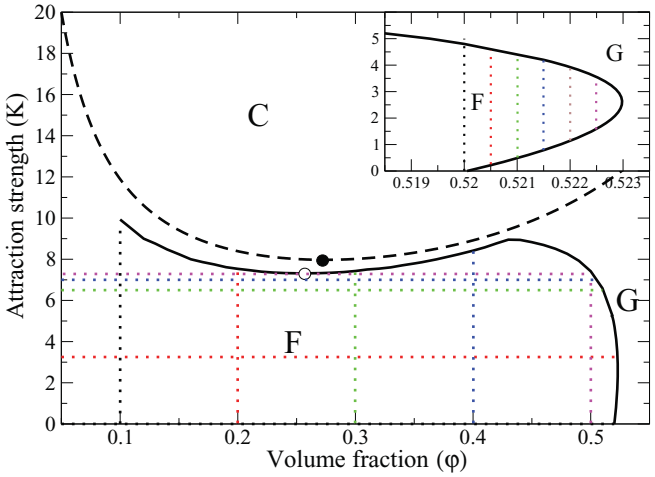

FIG. 1. (Color online) Phase diagram for short-range attractive colloids interacting through a HCAY potential with screening parameter $b = 12$. The ordinate axis can also be seen as an inverse temperature axis (βK). The dashed line is the spinodal and the continuous black line is the gel-glass line. C indicates the two-phase coexistence region, F is the fluid state, and G is the arrested (attractive and repulsive) states. The filled circle (•) indicates the critical point and the empty circle (○) indicates the minimum of the "gel" line. Horizontal and vertical dotted lines indicate the explored cuts. The inset is a zoom on the reentrance of the glass transition with additional vertical cuts indicated by the dotted lines.

in the phase diagram of Fig. 1 by the horizontal dotted lines). Our first observation is that the Ψ_2 predicted by (31) is negative for all volume fractions, consistent with low-shear-rate experiments and simulations [1]. A further notable feature of these curves is the influence of the critical point on the viscosity and the normal-stress coefficients. Whereas the viscosity η_0 seems to be largely unaffected by the proximity to the critical point, both Ψ_1 and $-\Psi_2$ present a maximum for volume fractions around 0.25. We recall that our present approach does not include the effects of hydrodynamic interactions—which are known to have a significant effect upon the low-shear viscosity in the vicinity of the critical point [47]—and thus provide only the structural contribution. The extent of the influence of solvent hydrodynamics on the normal-stress coefficients is, to the best of our knowledge, completely unknown, but the present results indicate that the structural contribution to these material functions becomes significantly enhanced in the critical region. At higher volume fractions, away from the critical point, we expect that hydrodynamic interactions will be less important and that the structural component considered here will dominate.

In order to obtain better insight into the microscopic length scales responsible for the macroscopic rheological functions shown in Fig. 2, we show in Fig. 3 the wave-vector-dependent integrands,

$$I_{\eta_0}(k) = \frac{1}{60\beta\pi^2}k^4\left(\frac{S_k'}{S_k}\right)^2\int_0^\infty dt\,\Phi_k^2(t), \tag{32}$$

$$I_{\Psi_1}(k) = \frac{1}{30\beta\pi^2}k^4\left(\frac{S_k'}{S_k}\right)^2\int_0^\infty dt\,\Phi_k^2(t)t, \tag{33}$$

$$I_{\Psi_2}(k) = \frac{1}{210\beta\pi^2}k^4\left(\frac{S_k'}{S_k^2}\right)(kS_k'' - S_k')\int_0^\infty dt\,\Phi_k^2(t)t, \tag{34}$$

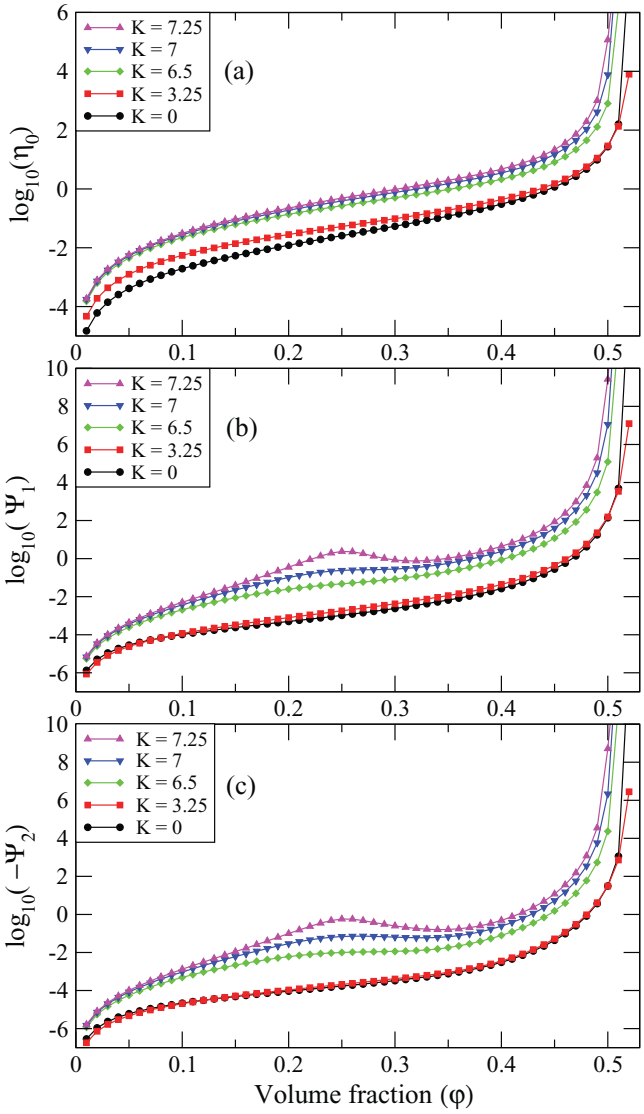

FIG. 2. (Color online) Zero-shear-rate limit of (a) the viscosity η_0, (b) the first normal-stress coefficient Ψ_1, and (c) the second normal-stress coefficient Ψ_2 as a function of the volume fraction φ, for different values of the potential depth K. These graphs correspond to the paths indicated by the horizontal dotted lines in Fig. 1.

over which we integrate to obtain η_0, Ψ_1, and Ψ_2. The curves shown in Figs. 3(a)–3(c) have been calculated at a fixed potential depth ($K = 7.25$) and for volume fractions over the range $\varphi = 0.15$–0.35. In Fig. 3(d), we show the integral $k_G \equiv \int dk k I_\alpha(k) / \int dk I_\alpha(k)$, where $\alpha = \{\eta_0, \Psi_1, \Psi_2\}$, for the different volume fractions considered. This integral measure makes clear the fact that at around $\varphi = 0.25$ (namely, close to the critical point, indicated by the arrow in the figure), the wave vectors contributing the most to both Ψ_1 and Ψ_2 are at $k_G \approx 0$. One can thus conclude that the first and second normal-stress coefficients in the vicinity of the critical point are dominated by long-range spatial correlations. In contrast, for the viscosity, the value of k_G remains at relatively large values, namely, $8.9 < k_G < 16.1$, which lie above the main peak (located around $2\pi/\sigma$) of the static structure factor ($k \approx 7$). These findings are consistent with the fact that hydrodynamics

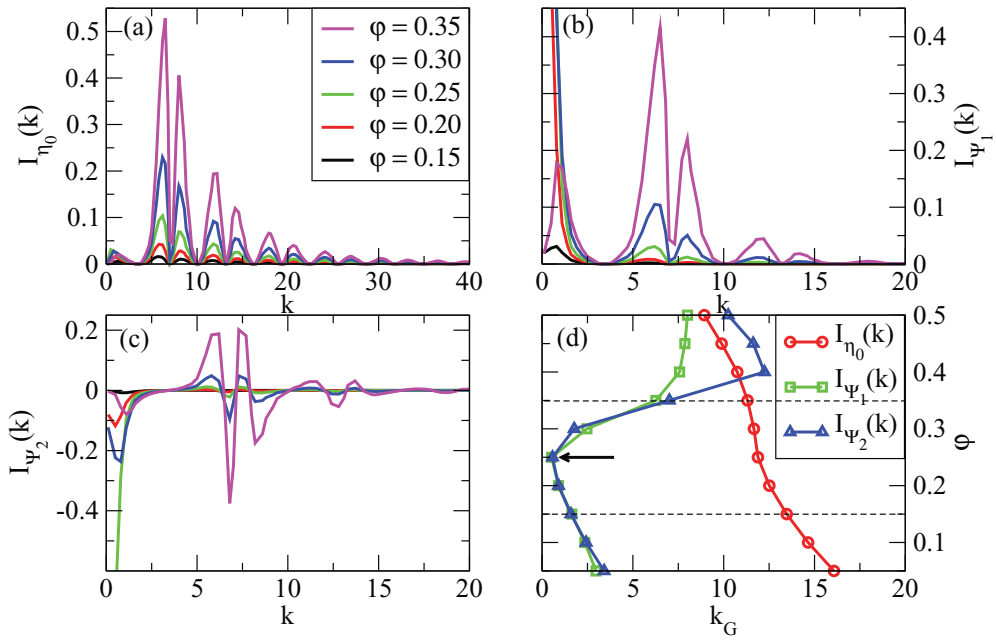

FIG. 3. (Color online) Integrands of (a) the viscosity η_0, (b) the first normal-stress coefficient Ψ_1, and (c) the second normal-stress coefficient Ψ_2, for volume fractions $\varphi = \{0.15, 0.20, 0.25, 0.30, 0.35\}$ and an attractive strength $K = 7.25$. (d) Plot of the weighted wave vectors k_G corresponding to the different volume fractions φ. The horizontal dashed lines indicate the range of volume fractions considered in (a)–(c), whereas the left arrow indicates the locus corresponding to the critical point.

interactions can become very important in the vicinity of the critical point [47] because the structural contribution is not dominated by long wavelength fluctuations, and supports our implicit assumption that the structural component considered here provides the main contribution to the normal-stress coefficients.

We return now to the macroscopic quantities. At first sight, the curves for Ψ_1 and Ψ_2 in Figs. 2(b) and 2(c) look qualitatively very similar and it might be expected that the ratio $Q \equiv -\Psi_1/\Psi_2$ will not vary as a function of volume fraction, for a given potential depth K. However, as shown in Fig. 4, this is not the case and the ratio Q exhibits significant structure. As mentioned in Sec. I, a lower boundary to Q of around 3 is to be anticipated on the basis of the available experimental data [1]. We find that Q remains bounded between approximately 3.4 and 13.0 for all volume fractions. One of the most striking features of the curves shown in Fig. 4 is that Q exhibits a global maximum at volume fractions $\varphi = 0.35$–0.4, for all values of the attraction strength investigated, thus indicating the volume fractions for which Ψ_1 is numerically most dominant over Ψ_2. This maximum reflects the increasing influence of packing effects and the slowing of structural relaxation with increasing volume fraction, although a clear physical interpretation remains elusive. What we observe is that the position (in volume fraction) of the global maximum can be correlated with the location of the glass transition boundary shown in Fig. 1. The influence of the reentrant glass transition is visible when considering the position of the maxima of Q: From $K = 0$ to $K = 6.5$, the maxima are shifted to lower values of the volume fraction, whereas for $K > 6.5$, they are shifted back to greater values. Although calculations performed closer to the critical point are numerically more demanding than at other points in the parameter space, the "bumps" appearing in Figs. 2(b) and 2(c) in the curves approaching the critical point are numerically robust.

In Figs. 5 and 6, we show the viscosity and normal-stress coefficients as a function of the attraction strength for various values of the volume fraction (vertical paths depicted in the phase diagram of Fig. 1). In Fig. 5(a), η_0 develops a minimum at high volume fraction, whereas in Figs. 5(b) and 5(c), both Ψ_1 and Ψ_2 exhibit a minimum not only at high volume fraction, but also at a low one ($\varphi = 0.1$), which is quite surprising given that at volume fraction $\varphi = 0.1$, the colloidal dispersion

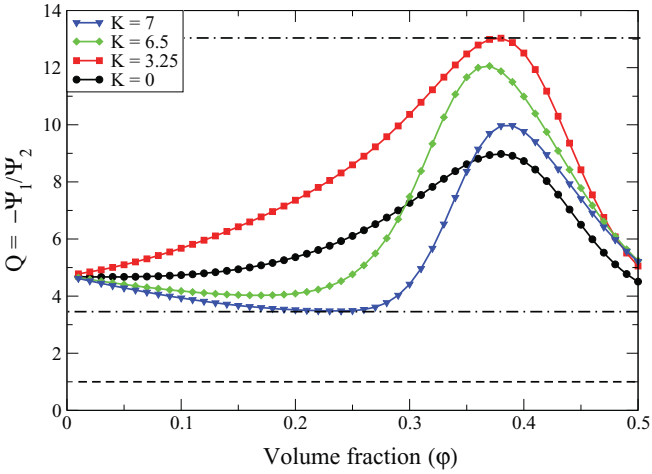

FIG. 4. (Color online) Ratio of the normal-stress coefficients ($Q = -\Psi_1/\Psi_2$) as a function of the volume fraction φ at different potential depth values K. A ratio $Q = 1$ is indicated by the horizontal dashed line. The other two horizontal dash-dotted lines at $Q \approx 3.4$ and $Q \approx 13.0$ indicate the lower and upper boundaries, respectively.

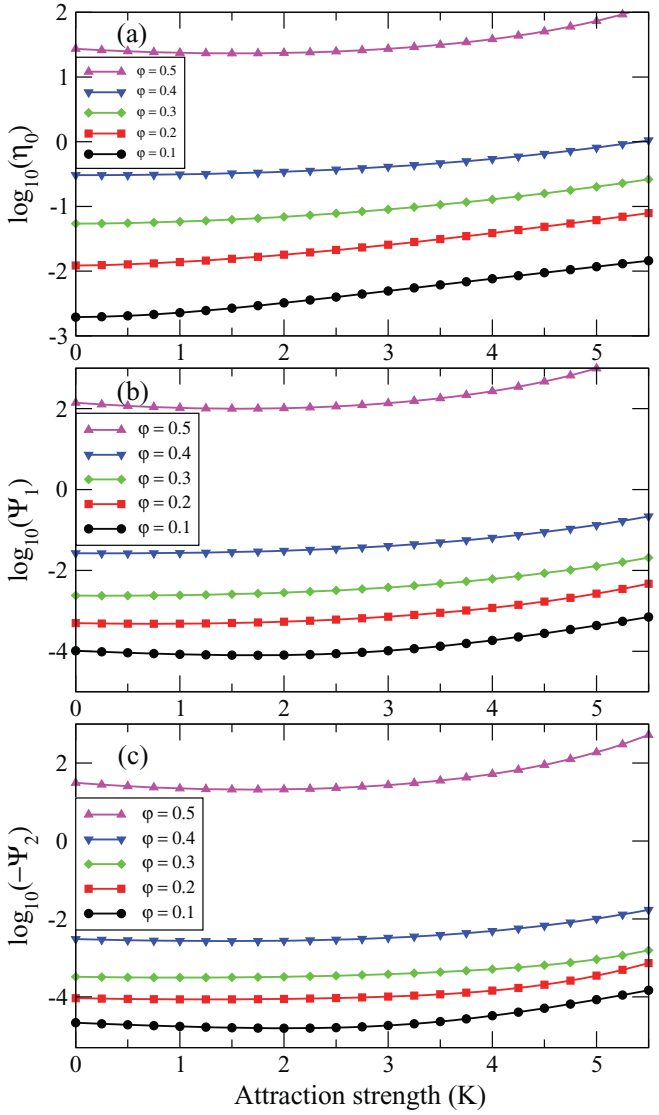

FIG. 5. (Color online) Zero-shear-rate limit of (a) the viscosity η_0, (b) the first normal-stress coefficient Ψ_1, and (c) the second normal-stress coefficient Ψ_2 as a function of the HCAY potential depth K, for different values of the volume fraction φ. These graphs correspond to the cuts indicated by the vertical dotted lines in Fig. 1.

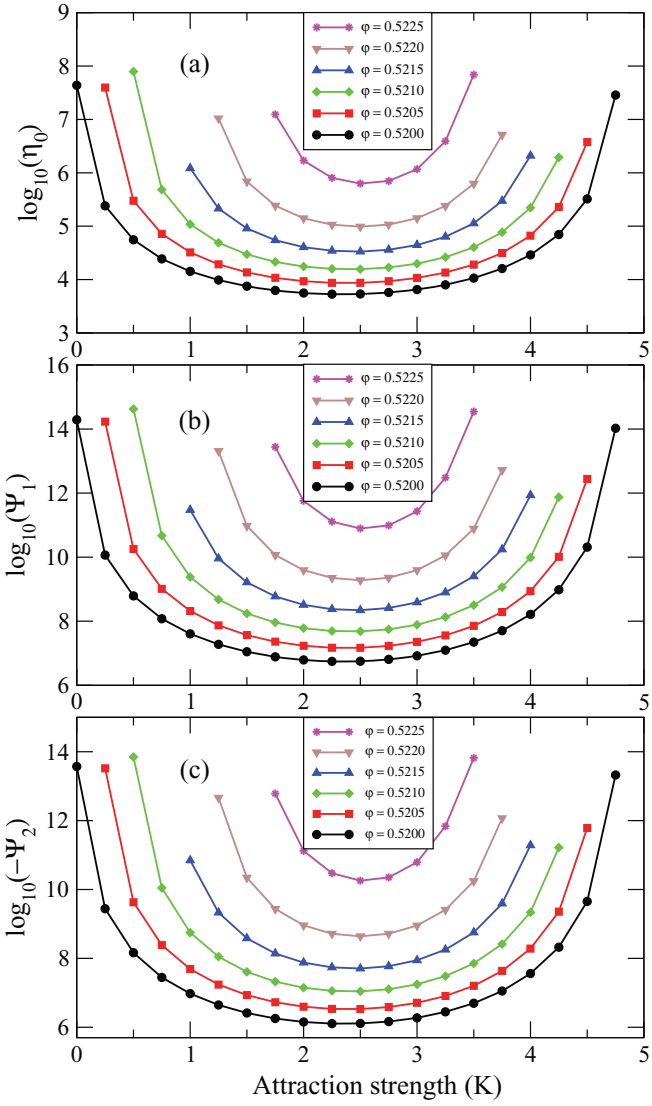

FIG. 6. (Color online) Zero-shear-rate limit of (a) the viscosity η_0, (b) the first normal-stress coefficient Ψ_1, and (c) the second normal-stress coefficient Ψ_2 as a function of the HCAY potential depth K, for different values of the volume fraction φ. These graphs correspond to the cuts indicated by the vertical dotted lines in the inset of Fig. 1.

is far from the reentrant region of the phase diagram. The nonmonotonic variation of the rheological functions as a function of the attraction strength K and the development of a minimum become particularly pronounced in the vicinity of the reentrant glass transition, as is demonstrated in Fig. 6. In this high volume fraction region, the rheological functions vary by many orders of magnitude over the range of K values investigated. All the minima in Fig. 6 lie at around $K \approx 2.6$, which corresponds to the highest value of the critical volume fraction (see Fig. 1).

To the best of our knowledge, neither experimental nor simulation data are available yet for normal-stress coefficients in the case of attractive Brownian particles. However, purely repulsive hard-sphere systems have been theoretically investigated and numerically simulated [3,12,48]. For dilute systems at low Peclet number, Brady and Vicic [3] predicted normal-stress differences proportional to $\dot{\gamma}^2$, with $N_1 > 0$ and $N_2 < 0$, clearly consistent with our formulas (30) and (31). Moreover, they found that both N_1 and N_2 scale with φ^2, which is exactly the behavior predicted by the present theory (see Fig. 7) at $K = 0$ and low volume fractions ($0 < \varphi < 0.15$). Concerning the ratio $Q = -\Psi_1/\Psi_2$, the discrepancy between their value, namely, 1.141, and our value, 4.67, can be attributed to the different approximations employed in the respective approaches. The theoretical predictions made by Nazockdast and Morris [48] at high volume fractions show that the normal-stress coefficients Ψ_1 and $-\Psi_2$ are stronger functions of the volume fraction than the zero-shear viscosity η_0, in agreement with Brady and Vicic [3] who predicted $\eta_0/\dot{\gamma} \sim [1-(\varphi/\varphi_m)]^{-2}$ and $\Psi_{1,2}/\dot{\gamma}^2 \sim [1-(\varphi/\varphi_m)]^{-3}$, where $\varphi_m \approx 0.63$ is the random close-packing volume fraction. We can make the same qualitative statement as Nazockdast and Morris about the behavior of our rheological functions. Moreover, we

find the exponents for the divergence of η_0, Ψ_1, and $-\Psi_2$ (with the critical volume fraction $\varphi^* = 0.5200527$) to be -2.55, -5.11, and -5.22, respectively.

Previous numerical studies of attractive colloidal particles interacting via square-well or Asakura-Osawa potentials have shown pronounced nonmonotonic behavior of both the self-diffusion coefficient [49] and the viscosity [50]. However, none of the previous works have reported normal-stress coefficients, despite their relevance for understanding the rheology of dispersions.

C. The rod-climbing effect

As mentioned in Sec. I, one striking manifestation of the normal-stress differences in viscoelastic liquids is the phenomenon of rod climbing (also called the Weissenberg effect) or rod dipping [2,4–8]. Indeed, when a rotating rod is vertically immersed in a liquid, the latter either climbs or move downwards along the cylinder because the shearing of the liquid induces stresses both in the gradient and the vorticity directions. These normal stresses are greater where the shear stress is largest, namely, in the vicinity of the rotating rod, and since the surface of the liquid is free, the liquid is forced to move up or down along the cylinder. It is clear that a rotating rod immersed into a Newtonian liquid will induce a negative surface deflection (or dipping) due to centrifugal forces, but without additional contributions from the normal stresses, since $N_1 = 0 = N_2$ for Newtonian liquids.

Polymer solutions have $N_1 > 0$ and $N_2 < 0$, and it is the rod climbing which is observed in such viscoelastic liquids. On the contrary, dispersions of non-Brownian particles present both $N_1 < 0$ and $N_2 < 0$ (both proportional to $\dot\gamma$ rather than to $\dot\gamma^2$), and rod dipping is actually observed [51,52]. As we will see below, the quantity determining whether a viscoelastic liquid will climb or dip is actually a linear combination of Ψ_1 and Ψ_2, called the climbing constant and denoted by $\hat\beta$. In the present case of attractive colloidal dispersions, we will see that although Ψ_1 is always positive and Ψ_2 is always negative, the resulting climbing constant $\hat\beta$ can change its sign from positive (rod climbing) to negative (rod dipping), or vice versa, when approaching the critical point.

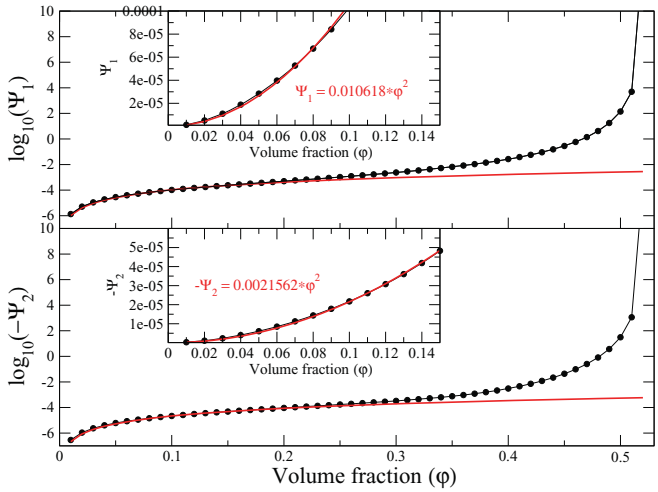

FIG. 7. (Color online) First (top) and second (bottom) normal-stress coefficients for pure hard spheres ($K = 0$). The red curves are fitted to the black dots in the range $0 < \varphi < 0.15$. The insets focus on the restricted volume fraction range, with linear-linear axes.

The theory of rod climbing, as well as its application to measurements of the normal-stress coefficients at low-shear rates, was developed by Joseph and his collaborators [7,8,10]. In this theory, the steady flow profile of a general viscoelastic fluid is given as a perturbation expansion in powers of the angular velocity Ω of the rod. The first deviation of the free surface from the static profile (due to wetting) arises at second order $O(\Omega^2)$ and is given by the following boundary-value problem:

$$\frac{\mathcal{T}}{r}(rh_2')' - \rho g h_2 - \frac{\rho a^4}{r^2} + \frac{4a^4\hat\beta}{r^4} = 0, \quad a < r < \infty, \tag{35a}$$

$$h_2'(a) = 0, \tag{35b}$$

$$(h_2, h_2') \overset{r\to\infty}{\longrightarrow} (0,0), \tag{35c}$$

where $h_2(r)$ is the aforementioned height of the fluid induced by the rotation of the rod, r is the distance from the center of the rod of radius a, g is the gravitational acceleration, and the dash represents a derivative with respect to r. The displacement of the fluid free surface will generate tensile forces in the surface film. These forces are captured by the first term of (35a), where $\mathcal{T}$ is the surface tension. In the absence of surface tension, the height $h_2(r)$ of the fluid arises from two distinct contributions. One of these is given by the third term in (35a) and would exist in the description of a Newtonian fluid: it represents a depression of the surface due to centrifugal forces, with ρ being the mass density of the fluid. The other contribution, given by the fourth term of (35a), accounts for the non-Newtonian nature of the fluid and describes the climbing (or dipping) along the rod. The climbing constant $\hat\beta$ is defined as $\hat\beta \equiv (\Psi_1 + 4\Psi_2)/2$ and is thus an intrinsic property of the fluid.[4] A non-Newtonian fluid will climb a rotating rod if $\hat\beta > 0$. If the surface tension $\mathcal{T}$ is neglected, it can be easily shown from the modified equation (35a) that the fluid only climbs below a critical radius, $r_c = 2\sqrt{\hat\beta/\rho}$.

When the rod is at rest ($\Omega = 0$), the static rise $h_s(r)$ of the liquid on the rod due to wetting is described by the following boundary-value problem:

$$\left(\frac{rh_s'}{\sqrt{1+h_s'^2}}\right)' - rSh_s = 0, \tag{36a}$$

$$h_s'(a) = -m, \tag{36b}$$

$$(h_s, h_s') \overset{r\to\infty}{\longrightarrow} (0,0), \tag{36c}$$

where $S \equiv \rho g/\mathcal{T}$ and $-m$ is the slope of the free surface at the rod, with the contact angle α being defined as $\tan^{-1}(-m)$. In the theory of Joseph *et al.*, the height of the fluid (with respect to the level of its free surface far from the rod at rest) is therefore given by the series

$$h(r;\Omega,m) = h_s(r;m) + h_{2,0}(r)\Omega^2/2 + \cdots, \tag{37}$$

[4] As mentioned in [8], it can be shown that by neglecting wetting, a free surface on the sheared liquid between parallel planes will never climb. Large radial gradients of the azimuthal shear stress are necessary to induce climbing.

with $h_2(r) \equiv h_{2,0}(r)$ and where the leading terms of higher order are

$$h_{2,1}(r)m\Omega^2/2 + h_{4,0}\Omega^4/4! + \cdots. \tag{38}$$

A good approximation to the expansion (37) is given by the truncation

$$h(r;\Omega,m) \sim h_s(r;m) + h_2(r)\Omega^2/2, \tag{39}$$

with this latter being valid while $\omega^4 a < 144$, with the frequency $\omega = \Omega/(2\pi)$. If this condition is no longer fulfilled, then higher-order terms in the expansion (37) must be considered. In the following, we will present results satisfying the condition $\omega^4 a < 144$. The theoretical surface profiles are thus computed from

$$h(r;a,\omega^2,\hat{\beta},m) = h_s(r;a,m) + 2\pi^2\omega^2 h_2(r;a;\hat{\beta}), \tag{40}$$

where $h_s(r;a,m)$ and $h_2(r;a;\hat{\beta})$ obey to the boundary-value problems (36) and (35), respectively. The theory of Joseph *et al*. thus presents a useful way to determine experimentally the normal-stress coefficients by identifying the slope of the plot of the total height at the rod surface, $h(a)$, with respect to the rotational frequency of the rod. Once this slope is known, the climbing constant $\hat{\beta}$ can then be calculated from the relation

$$\frac{dh}{d\omega^2} = \frac{2\pi^2 a}{T\sqrt{S}}\left[\frac{4\hat{\beta}}{4+\lambda} - \frac{\rho a^2}{2+\lambda}\right], \tag{41}$$

where $\lambda \equiv a\sqrt{S}$, and finally the normal-stress coefficients can be obtained [10]. In Fig. 8, we attempt to give some feeling for the influence of the sign of the climbing constant $\hat{\beta}$ on the free-surface profile.

Our derivation of the normal-stress coefficients Ψ_1 and Ψ_2 at low-shear rates allows us to calculate the climbing constant $\hat{\beta}$ and make predictions for the climbing (or dipping) of hard-sphere or attractive colloidal dispersions. In Fig. 9, we show the variation of $\hat{\beta}$ with volume fraction φ for the HCAY system

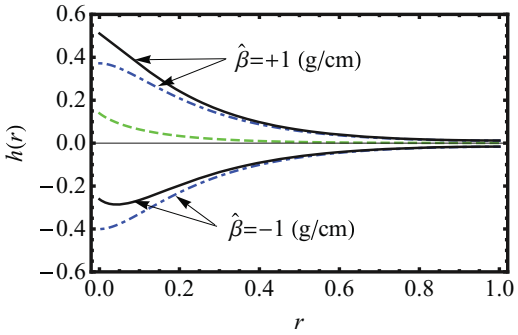

FIG. 8. (Color online) Height $h(r)$ (cm) of the free surface of the fluid with respect to the distance r (cm) from the rod, for two values of the climbing constant $\hat{\beta}$ (g/cm). $r = 0$ corresponds to the rod surface. The green dashed line is the static deflection $h_s(r)$ due to wetting and the blue dash-dotted lines correspond to the contribution arising from the rotating rod, namely, $2\pi^2\omega^2 h_2(r)$. The black continuous lines represent the total height of the fluid, $h(r) = h_s(r) + 2\pi^2\omega^2 h_2(r)$. Parameters: mass density $\rho = 0.88$ g/cm^3, surface tension $\mathcal{T} = 31$ g s^{-2}, rod radius $a = 0.32$ cm, contact angle $m = \tan 55^\circ$, and rotation frequency $\omega = 3.8$ rev/s.

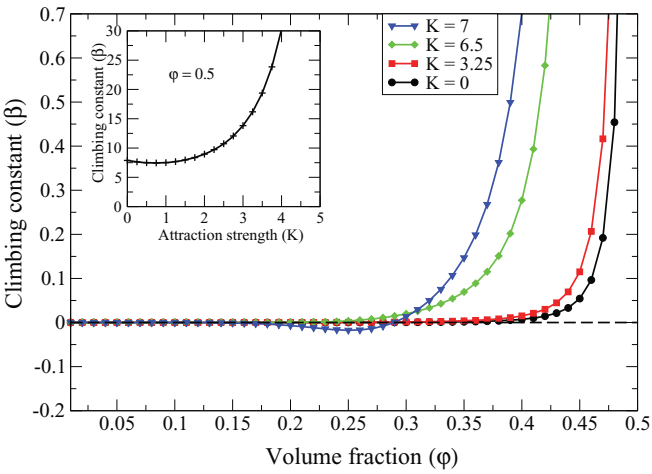

FIG. 9. (Color online) Climbing constant $\hat{\beta}$ with respect to the volume fraction φ at different potential depths K. The horizontal dashed line indicates $\hat{\beta} = 0$. The inset shows the influence of the glass transition reentrance on $\hat{\beta}$ with respect to K, at a volume fraction close to the glass transition.

at different attraction strengths K.[5] Although the curves with $K = 0$, $K = 3.25$, and $K = 6.5$ remain monotonic, the one with $K = 7$ displays increased structure, due to the proximity to the critical point (see phase diagram of Fig. 1). We thus predict that a dispersion of hard-sphere or weakly attractive Brownian particles will climb up a rotating rod (although larger volume fractions are required to get significant climbing for smaller values of K) and that rod dipping will occur when approaching the critical point. As can be seen in the inset of Fig. 9, at large volume fractions, e.g., $\varphi = 0.5$, the climbing constant $\hat{\beta}$ takes much larger values, even for $K = 0$. Moreover, at these dense values, $\hat{\beta}$ develops a minimum because of the influence of the reentrant glass transition and is thus relatively less important at potential depths around $K \approx 0.75$.

In order to get a better insight regarding the magnitude of the climbing (or dipping) effect, we choose a set of realistic values for the different parameters (solvent density $\rho_{\text{solv}} = 0.88$ g/cm^3,[6] surface tension $\mathcal{T} = 31$ g s^{-2}, rod radius $a = 0.32$ cm, contact angle $m = \tan 55^\circ$, and rotation frequency $\omega = 3.8$ rev/s) rather than working with dimensionless quantities, and we calculate from (40) the surface profiles for three different situations depicted in Figs. 10–12. We point out that the following results for the surface profiles should be considered as qualitative, rather than quantitative, indications of the physical phenomenon.

Figure 10 shows that rod climbing occurs even in the case of hard-sphere colloidal dispersions, provided that the volume fraction is large enough. With our chosen parameters, the fluid climbs up to around 1.5 cm at $\varphi = 0.48$, which represents about 15 times the height at the rod due to wetting (see the

[5] In Fig. 9, SI units are implicitly assumed for $\hat{\beta}$, namely, kg/m.

[6] For a dispersion of density matched colloids in a solvent, the total mass density is given by $\rho = \rho_{\text{solv}}(1+\varphi)$. We thus choose $\rho_{\text{solv}} = 0.88$ g/cm^3.

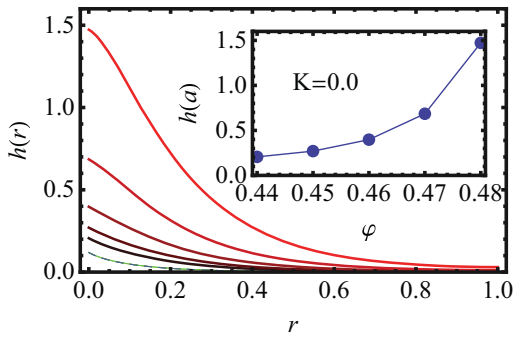

FIG. 10. (Color online) Height $h(r)$ (cm) of the free surface of the fluid with respect to the distance r (cm) from the rod, for a colloidal dispersion of hard spheres at volume fractions ranging from $\varphi = 0.44$ (black lines) to $\varphi = 0.48$ (red lines). The green dashed lines indicate the static climbing. Inset: total height at the rod. See text for chosen parameters.

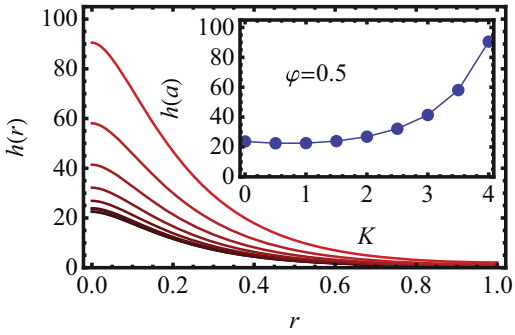

FIG. 12. (Color online) Height $h(r)$ (cm) of the free surface of the fluid with respect to the distance r (cm) from the rod, for a dense dispersion of short-range attractive colloidal particles interacting via the HCAY potential. The volume fraction φ is set to 0.5. The potential depth varies from $K = 0$ (black lines) to $K = 4$ (red lines), with a step size of 0.5. Inset: total height at the rod. See text for chosen parameters.

green dashed curves). Figure 11 exhibits surface profiles of a semidense dispersion of colloidal particles strongly interacting via the HCAY potential with $K = 7$. Within the range $\varphi \approx 0.15$–0.3, the climbing constant becomes negative (see Fig. 9), which results in rod dipping: the surface profiles lie below those due to wetting alone. This rod-dipping region is induced by the proximity to the critical point. For $\varphi > 0.3$, the climbing constant becomes positive and increases monotonically, such that the fluid climbs up the rod. Finally, Fig. 12 shows the surface profiles of a dense colloidal dispersion ($\varphi = 0.5$) for different attraction strengths. At such a high volume fraction, the elastic component of the dispersion is significant enough to give rise to very strong rod climbing. Thus, although most of the experiments showing rod climbing have been realized with polymeric fluids, the Weissenberg effect is also very prominent in colloidal dispersions. A decisive factor in determining the magnitude of the effect is the strength of the elastic contribution to the viscoelastic response.

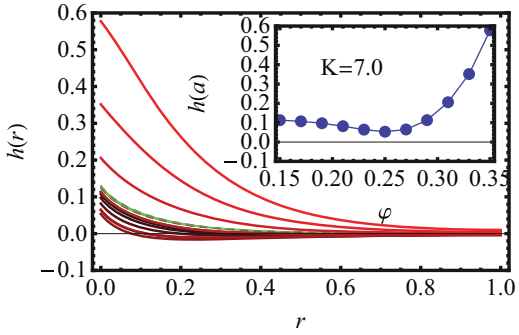

FIG. 11. (Color online) Height $h(r)$ (cm) of the free surface of the fluid with respect to the distance r (cm) from the rod, for a dispersion of short-range attractive colloidal particles interacting via the HCAY potential. The potential depth is set to $K = 7$. Volume fractions range from $\varphi = 0.15$ (black lines) to $\varphi = 0.35$ (red lines), with a step size of 0.02. The green dashed lines indicate the static climbing. Inset: total height at the rod. See text for chosen parameters.

IV. CONCLUSION AND OUTLOOK

In this paper, we have shown how the mode-coupling constitutive equation (17) can be used to develop expressions [Eqs. (30) and (31)] for the first and second normal-stress coefficients, opening a path for these important material constants to be calculated from first principles. Given the system volume fraction and static structure factor, our theory enables us to bridge the gap between macroscopic rheological phenomena, such as the rod-climbing effect, and the underlying microscopic interactions. Although we have neglected the influence of hydrodynamic interactions, we anticipate that these will be considerably less important for determining the normal-stress coefficients than for the shear viscosity (where hydrodynamic effects are known to be important close to the critical point [47]). The theory developed here should thus reliably predict the phenomenology of normal stresses and rod climbing, although we anticipate quantitative errors as a result of our various approximations.

When our mode-coupling expressions are used as input to the Joseph *et al.* theory of rod climbing, we can make first-principles predictions for the surface profile of dispersions in a Couette rheometer. Qualitative changes in the profile as a function of thermodynamic state point can then be investigated in a systematic fashion. This is somewhat contrary to the usual experimental practice of determining the interface profile and then using this information to infer the normal-stress coefficients. It would be of considerable interest to compare our theoretical predictions with data from either experiments or simulations on attractive colloids in order to test the qualitative trends. Work along these lines is currently in progress.

In contrast to shear flow, for which η_0, Ψ_1, and Ψ_2 are all highly relevant, strong flows are characterized entirely by the extensional viscosity $\eta_{\text{ext}} \equiv (\sigma_{xx} - \sigma_{yy})/\dot{\epsilon}$, where the stress components σ_{xx} and σ_{yy} are those corresponding to an extensional flow whose extensional strain rate is expressed by $\dot{\epsilon}$. In agreement with the Trouton rules, we verified that $\eta_{\text{ext}} = 3\eta_0$, which provides an additional check for the consistency of the constitutive equation (17) arising from the ITT-MCT formalism.

The present work has addressed rod climbing as a manifestation of normal-stress differences. However, these "hoop stresses" have also been implicated in the onset of rolling flow in bulk and may lie at the origin of vorticity banding [53]. Whether the present theory can predict the onset of such inhomogeneous flow remains a topic for future research.

ACKNOWLEDGMENTS

We thank Th. Voigtmann for providing numerical code for the solution of the MCT equations. This work was supported by the Swiss National Science Foundation.

[1] R. G. Larson, *The Structure and Rheology of Complex Fluids* (Oxford University Press, New York, USA, 1999).
[2] J. Mewis and N. Wagner, *Colloidal Suspension Rheology* (Cambridge University Press, Cambridge, UK, 2012).
[3] J. F. Brady and M. Vicic, J. Rheol. **39**, 545 (1995).
[4] K. Weissenberg, Nature (London) **159**, 310 (1947).
[5] C. W. Macosko, *Rheology: Principles, Measurements, and Applications* (Wiley-VCH, New York, USA, 1994).
[6] R. B. Bird, R. C. Armstrong, and O. Hassager, *Dynamics of Polymeric Liquids* (Wiley, New York, 1987), Vol. 1.
[7] D. D. Joseph and R. L. Fosdick, Arch. Rational Mech. Anal. **49**, 321 (1973).
[8] D. D. Joseph, G. S. Beavers, and R. L. Fosdick, Arch. Rational Mech. Anal. **49**, 381 (1973).
[9] R. G. Larson, *Constitutive Equations for Polymer Melts and Solutions* (Butterworths, London, 1988).
[10] D. D. Joseph, G. S. Beavers, A. Cers, C. Dewald, A. Hoger, and P. T. Than, J. Rheol. **28**, 325 (1984).
[11] A. S. Khair and T. M. Squires, Phys. Rev. Lett. **105**, 156001 (2010).
[12] J. Bergenholtz, J. Brady, and M. Vicic, J. Fluid Mech. **456**, 239 (2002).
[13] D. R. Foss and J. F. Brady, J. Fluid Mech. **407**, 167 (2000).
[14] M. Lee, M. Alcoutlabi, J. Magda, C. Dibble, M. Solomon, X. Shi, and G. McKenna, J. Rheol. **50**, 293 (2006).
[15] J. F. Brady and G. Bossis, J. Fluid Mech. **155**, 105 (1985).
[16] X. Cheng, J. H. McCoy, J. N. Israelachvili, and I. Cohen, Science **333**, 1276 (2011).
[17] A. Montesi, A. A. Peña, and M. Pasquali, Phys. Rev. Lett. **92**, 058303 (2004).
[18] P. A. Janmey, M. E. McCormick, S. Rammensee, J. Leight, P. C. Georges, and F. C. MacKintosh, Nat. Mater. **6**, 48 (2006).
[19] J. M. Brader, J. Phys.: Condens. Matter **22**, 363101 (2010).
[20] J. K. G. Dhont, *An Introduction to Dynamics of Colloids* (Elsevier, Amsterdam, 1996).
[21] D. Ronis, Phys. Rev. A **29**, 1453 (1984).
[22] D. Ronis, Phys. Rev. A **34**, 1472 (1986).
[23] M. Fuchs and M. E. Cates, Phys. Rev. Lett. **89**, 248304 (2002).
[24] J. M. Brader, T. Voigtmann, M. E. Cates, and M. Fuchs, Phys. Rev. Lett. **98**, 058301 (2007).
[25] J. M. Brader, M. E. Cates, and M. Fuchs, Phys. Rev. Lett. **101**, 138301 (2008).
[26] J. M. Brader, M. E. Cates, and M. Fuchs, Phys. Rev. E **86**, 021403 (2012).
[27] O. Henrich, F. Weysser, M. E. Cates, and M. Fuchs, Phil. Trans. R. Soc. A **367**, 5033 (2009).
[28] M. Krüger, F. Weysser, and M. Fuchs, Eur. Phys. J. E **34**, 88 (2011).
[29] M. Fuchs and M. E. Cates, Faraday Discuss. **123**, 267 (2003).
[30] J. M. Brader, T. Voigtmann, M. Fuchs, R. G. Larson, and M. E. Cates, Proc. Nat. Acad. Sci. USA **106**, 15186 (2009).
[31] J. M. Brader, M. Siebenbürger, M. Ballauff, K. Reinheimer, M. Wilhelm, S. J. Frey, F. Weysser, and M. Fuchs, Phys. Rev. E **82**, 061401 (2010).
[32] T. F. F. Farage and J. M. Brader, J. Rheol. **56**, 259 (2012).
[33] T. Voigtmann, J. M. Brader, M. E. Cates, and M. Fuchs, Soft Matter **8**, 4244 (2012).
[34] M. Ballauff, J. M. Brader, S. U. Egelhaaf, M. Fuchs, J. Horbach, N. Koumakis, M. Krüger, M. Laurati, K. J. Mutch, G. Petekidis, M. Siebenbürger, T. Voigtmann, and J. Zausch, Phys. Rev. Lett. **110**, 215701 (2013).
[35] K. N. Pham, A. M. Puertas, J. Bergenholtz, S. U. Egelhaaf, A. Moussaid, P. N. Pusey, A. B. Schofield, M. E. Cates, M. Fuchs, and W. C. K. Poon, Science **296**, 104 (2002).
[36] G. Nägele and J. Bergenholtz, J. Chem. Phys. **108**, 9893 (1998).
[37] L. D. Landau and E. M. Lifshitz, *Theory of Elasticity* (Elsevier-Butterworth-Heinemann, New York, 1986).
[38] M. Doi and S. F. Edwards, *The Theory of Polymer Dynamics* (Oxford University Press, New York, 1989).
[39] N. J. Wagner, Phys. Rev. E **49**, 376 (1994).
[40] J. K. G. Dhont, J. Fluid Mech. **204**, 421 (1989).
[41] F. Sciortino and P. Tartaglia, Adv. Phys. **54**, 471 (2005).
[42] R. Mezzenga, P. Schurtenberger, A. Burbidge, and M. Michel, Nat. Mater. **4**, 729 (2005).
[43] G. Foffi, G. D. McCullagh, A. Lawlor, E. Zaccarelli, K. A. Dawson, F. Sciortino, P. Tartaglia, D. Pini, and G. Stell, Phys. Rev. E **65**, 031407 (2002).
[44] J. Bergenholtz and M. Fuchs, Phys. Rev. E **59**, 5706 (1999).
[45] J.-P. Hansen and I. R. McDonald, *Theory of Simple Liquids* (Academic, London, 1986).
[46] T. Voigtmann, Ph.D. thesis, Technische Universität München, 2003.
[47] J. K. G. Dhont and G. Nagele, Phys. Rev. E **58**, 7710 (1998).
[48] E. Nazockdast and J. F. Morris, J. Fluid Mech. **713**, 420 (2012).
[49] E. Zaccarelli, G. Foffi, K. A. Dawson, S. V. Buldyrev, F. Sciortino, and P. Tartaglia, Phys. Rev. E **66**, 041402 (2002).
[50] A. M. Puertas, C. D. Michele, F. Sciortino, P. Tartaglia, and E. Zaccarelli, J. Chem. Phys. **127**, 144906 (2007).
[51] I. E. Zarraga, D. A. Hill, and D. T. Leighton, J. Rheol. **44**, 185 (2000).
[52] F. Boyer, O. Pouliquen, and E. Guazzelli, J. Fluid Mech. **686**, 5 (2011).
[53] J. K. G. Dhont and W. M. Briels, Rheol. Acta **47**, 257 (2008).